Silicon pseudo-Dirac nodal-sphere semimetal from high-throughput structure screening

Pinglan Yan,[1] Shifang Li,[1] Jin Li ![ORCID],[1,*] Chaoyu He,[1] Tao Ouyang,[1] Chao Tang,[1] and Jianxin Zhong[1,2,†]

[1]*Hunan Key Laboratory of Micro-Nano Energy Materials and Devices, Xiangtan University,*
Hunan 411105, People's Republic of China

and Laboratory for Quantum Engineering and Micro-Nano Energy Technology and School of Physics and Optoelectronics,
Xiangtan University, Hunan 411105, People's Republic of China

[2]*Institute for Quantum Science and Technology, Shanghai University, Shanghai 200444, People's Republic of China*

Dirac nodal sphere (DNS) semimetals possess unique electronic properties beyond the Dirac nodal points and Dirac nodal lines paradigm. However, Dirac nodal sphere semimetals are very rare in real materials as it is very difficult to realize with discrete crystal point group symmetries. In this work, a silicon structure (I4$_1$/acd-Si$_{80}$) with pseudo-Dirac nodal sphere (PDNS) is proposed via the high-throughput screening for silicon based on our RG^2 code and transferable tight-binding (TB) method from 2573 silicon allotropes. The results show that the pseudo-Dirac nodal sphere is around the Γ point with glide symmetries protected Dirac nodal loops (DNLs) on high-symmetry planes and tiny energy gap (<1 meV) at the general band crossing points. Our calculations of phonon spectrum, *ab initio* molecular dynamics, elastic constants, and formation energy show that I4$_1$/acd-Si$_{80}$ is a metastable phase of silicon. Furthermore, I4$_1$/acd-Si$_{80}$ exhibits interesting photoelectric properties with photoexcitable high-velocity Dirac fermions and has potential applications in Si-based photoelectric devices.

I. INTRODUCTION

Topological semimetals (TSM) have attracted numerous attention due to their exotic electronic properties and future application prospects [1–4]. Among topological semimetals, the Dirac nodal point, nodal line, nodal ring, and nodal surface TSMs have been investigated extensively [5–10]. Besides these TSMs, Dirac nodal sphere (DNS) or pseudo-DNS (PDNS) TSMs can be obtained when the linear band crossings form a closed surface [11–13]. Owing to the dimensionality of DNS, the nodal sphere semimetals have very unique electronic properties different with that of Dirac nodal point and nodal line TSMs, such as constant density of states (DOS), orientation independent drumhead surface states, and localized spin Hall conductivity, which make the nodal sphere semimetals have some unusual applications in quantum oscillation and plasmon excitations [12,13]. In pervious work, Wang *et al.* [12] demonstrated two possible types of PDNS states from crystal symmetries and identified the possible point groups for PDNS. Compared with other types of Dirac semimetals, the DNS semimetals are very rare and the understandings about the symmetric properties and material platforms of PDNS are also very limited. Up to now, there are only several robust PDNS proposed, such as MH$_3$ (M = Y, Ho, Tb, Nd) and Si$_3$N$_2$, [12] CaTe [13] and carbon nanotube networks [14]. It is of great interest to search new DNS materials and explore their properties.

Silicon, due to its tetracoordinated bonding characteristics, has numerous three-dimensional (3D) silicon metastable configurations besides the cubic-diamond structure. By applying and releasing pressure, there are several silicon metastables stabilized in ambient conditions, such as Si-III (BC8), Si-IV, Si-XII (R8), Si-VIII, and Si-IX [15]. Ramachandran *et al.* synthesized the alkali-free silicon clathrate Si$_{136}$ by vacuum heating and density separation from the Zintl phase NaSi [16]. Rapp *et al.* have obtained several silicon allotropes stable at ambient conditions including ST12, BT8, Si-VIII, t32, and t32* by employing ultrafast laser-induced confined microexplosion [17]. The open channels Si$_{24}$ was fabricated in experiments by several research groups with different methods [18–20]. In addition, many other silicon allotropes were predicted by theoretical calculations [21–27]. These experimental and theoretical works confirm the existence of numerous silicon allotropes and these silicon structures can provide rich electronic properties, including semiconductors [22–24], metals [15], and topological nodal-line semimetals (AHT-Si$_{24}$, VFI-Si$_{36}$ [26], and I4/mcm-Si$_{48}$ [27]). However, there is no DNS or PDNS TSM silicon reported up to now. Therefore, exploring silicon DNS or PDNS semimetal is of crucial importance for fundamental and practical interests due to its exotic properties and compatibility with semiconductor industry.

Most of the previous theoretical works proposed new silicon allotropes by reconstruction from known structures, genetic engineering and specific search algorithm, which usually generated a small number of candidates and are difficult to find desired new structures. Recently, the high-throughput screening method is illustrated to be a useful tool for searching and designing special functional materials in a more

---

*Contact author: lijin@xtu.edu.cn
†Contact author: jxzhong@shu.edu.cn

systematical way [28–30]. In this work, we have carried out the high-throughput screening for silicon by our RG^2 code [31] and the transferable DFT-HSE based tight-binding (TB) model [27,32,33], and identified a TSM silicon structure (I4$_1$/acd-Si$_{80}$) with PDNS near Fermi level from 2573 candidate silicon allotropes. For this silicon PNDS, it is found that the Dirac nodal loops on high-symmetry planes are protected by the glide symmetries according to the symmetric properties of the Bloch states and there are tiny band gaps (<1 meV) for the band crossing points off high symmetric lines. Furthermore, I4$_1$/acd-Si$_{80}$ possesses high Fermi velocity and has potential applications in Si-based high-speed photoelectric devices.

II. METHODS

In this work, thousands of four-coordinated silicon structures were generated by the RG^2 structure searching code [24,31], and these structures were optimized using by Vienna *ab initio* simulation package (VASP) [34]. The projector augmented wave [35] type of electron-ion interaction and Perdew-Burke-Ernzerhof type of exchange-correlation functional [36] are used in our first-principles calculations. A 500 eV cutoff energy is used for the expansion of plane-wave basis functions. The Brillouin-zone (BZ) integrations are performed with a uniform density Monkhorst-Pack *k* mesh ($2\pi \times 0.01$ Å^{-1}). All the structures are fully optimized by the conjugate gradient algorithm until the atomic force is smaller than 0.01 eV/Å. For DNS or PDNS semimetal, one of its most important feature is there are multiple Dirac-like band crossing points near Fermi level in the band structure. In order to find out the silicon allotropes with multiple band crossing points effectively, the high-throughput band structure calculations and screening have been performed by the general and transferable tight-binding (gt-TB) method for silicon [27], and the band structure of selected silicon allotropes are further calculated by Heyd-Scuseria-Ernzerhof (HSE) hybrid functional [37] and Wannier functions approach [38].

III. RESULTS AND DISCUSSION

To generate four-connected sp^3 silicon structures with bond lengths and angles close to that in diamond configuration (2.35 Å and 109°), the random method based on group and graph theory (RG^2) is employed. Crystal cells (3 Å $\leqslant$ *a*, *b*, *c* $\leqslant$ 18 Å; 30° $\leqslant$ α, β, γ $\leqslant$ 150°; No. 10 $\leqslant$ space group $\leqslant$ No. 230) and inequivalent atomic positions are randomly generated by RG^2 and all the other atomic positions are determined by the corresponding symmetries. RG^2 will calculate the distance matrix and build the four-adjacent quotient graph (QG) for each configuration according to the principle of proximity. The optimization of cell and atomic positions were performed by RG^2 under conservation of QG. Finally, the surviving candidates with accepted bond length [2.35±(0.18×2.35) Å] and angles [109° ± (0.25×109)°] will be further optimized through high-level DFT-based first-principles calculations. After removing the same structures and further relaxing by VASP, 2573 low-density silicon candidates were retained finally. In order to rapidly obtain the reliable electronic properties of so many silicon allotropes and
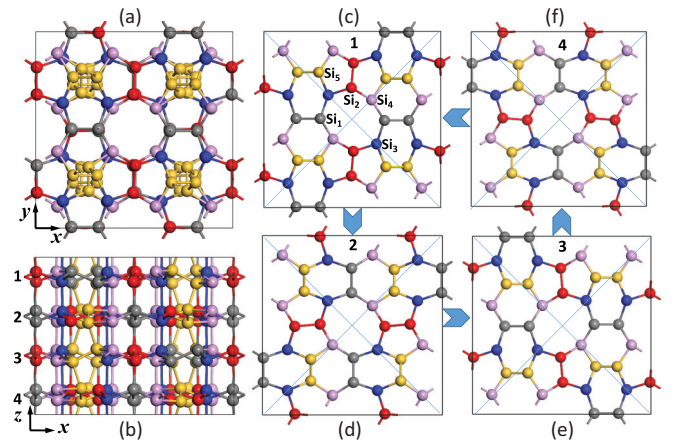
FIG. 1. Top (a) and side (b) views of the crystal structure of I4$_1$/acd-Si$_{80}$ in tetragonal cell. The five kinds of inequivalent Si atoms are denoted by different colors. (c)–(f) are the atomic geometries of the four layers.

avoid the time-consuming DFT-HSE calculations, we used the general and transferable tight-binding method with DFT-HSE based TB parameters for silicon to calculate the band structures. It is found that there are 2344 semiconductors, 211 metals, and 18 Dirac-like semimetals. By further analyzing the band structures of Dirac-like semimetals, one PDNS silicon structure was found, and thus we have studied the PDNS silicon structure in the following sections specially.

The primitive cell of the PDNS silicon is body-centered tetragonal with the I4$_1$/acd space group (No. 142) and contains 80 silicon atoms, thus we name it as I4$_1$/acd-Si$_{80}$ for short according to its structural characteristics. To show the crystal symmetry of I4$_1$/acd-Si$_{80}$ more clearly, the atomic structure in conventional cells is displayed in Figs. 1(a) and 1(b), and the lattice constants of conventional cells are $a = b = 16.239$ Å and $c = 12.877$ Å. In the cell, there are five inequivalent atoms at the positions (0.18, 0.0059, 0.906), (0.0052, 0.1817, 0.9089), (0.1388, 0.1363, 0.8469), (0.389, 0.109, 0.9086), and (0.2682, 0.1896, 0.9167). In I4$_1$/acd-Si$_{80}$, silicon atoms form tetragonal, pentagonal, hexagonal, and octagonal loops, which make the silicon density (2.19 g/cm^3) lower than that of diamond Si (2.28 g/cm^3). From the side view, one can see that I4$_1$/acd-Si$_{80}$ is formed by four silicon layers. It is found that the atomic configurations of the four layers are the same but with different orientation, as shown in Figs. 1(c)–1(f), and they are related by certain symmetric operations. For example, the first and third layers can be obtained by rotating the fourth and second layer by 90 degrees along the central axis perpendicular to the layer, while the second (fourth) layer can be obtained by the first (third) layer through the 180 degree rotation along the diagonal axes.

The stability of I4$_1$/acd-Si$_{80}$ is studied comprehensively. First, the phonon spectrum of I4$_1$/acd-Si$_{80}$ is calculated by PHONOPY code [39] associated with VASP as shown in Fig. 2(a). One can see that there is no imaginary frequency, which confirms that I4$_1$/acd-Si$_{80}$ is dynamically stable. The thermal stability is also studied by the *ab initio* molecular dynamics (AIMD) simulations in canonical ensemble for the conventional cell with 160 silicon atoms. After simulating for
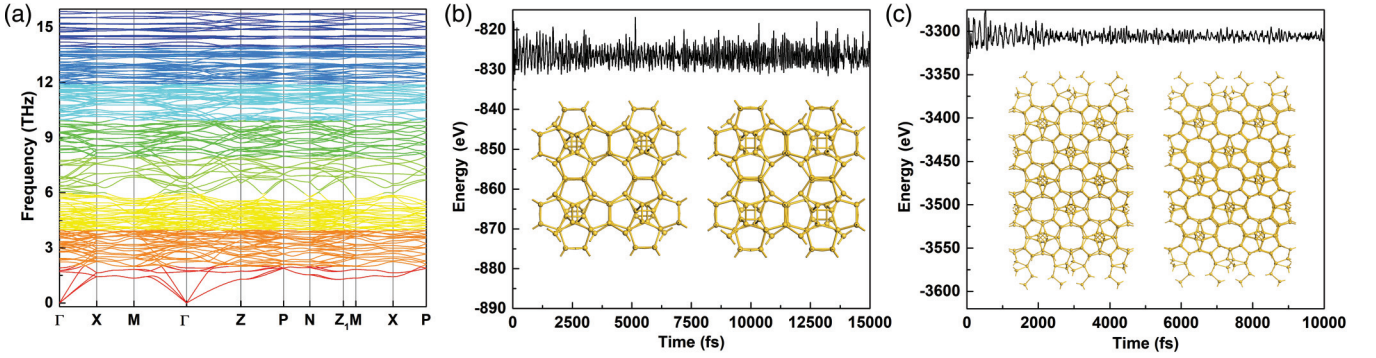
FIG. 2. (a) The phonon spectrum of $I4_1/acd$-Si_{80}. (b) The fluctuation of total energy and the final atomic structure of (b) 160 atoms supercell with 15 ps and (c) 640 atoms supercell with 10 ps at 300 K AIMD simulation.

15 ps at 300 K, the atomic structure of $I4_1/acd$-Si_{80} shows only small deformations and remains intact, and the total energy also oscillates in a small range without significant changes during the entire simulation [Fig. 2(b)], and similar results are also obtained for the AIMD calculation with 640 atoms supercell for 10 ps at 300 K [Fig. 2(c)], which suggests the good thermal stability of $I4_1/acd$-Si_{80} at room temperature. Furthermore, the elastic constants of $I4_1/acd$-Si_{80} are calculated and the results are $C_{11} = 112.11$ GPa, $C_{33} = 123.94$ GPa, $C_{44} = 31.95$ GPa, $C_{66} = 46.69$ GPa, $C_{12} = 69.62$ GPa, and $C_{13} = 41.52$ GPa, which satisfies the mechanical stability criteria of tetragonal phase [40]. In addition, the calculated formation energy of $I4_1/acd$-Si_{80} is -5.2 eV/atom, indicating that $I4_1/acd$-Si_{80} is a metastable phase as its formation energy is 0.22 eV/atom higher than that of diamond Si. However, it is important to note that metastable phases even with high-energy can be experimentally discovered or synthesized with appropriate methods if the phase is dynamical, thermal, and mechanical stable. For example, T-carbon [41,42], C21-sc carbon [43,44], graphdiyne [45,46], and biphenylene [47,48] have been fabricated experimentally, but their formation energies are about 1200 meV/atom, 500 meV/atom, 234 meV/atom, and 450 meV/atom higher than their corresponding ground states, respectively. Furthermore, the metastable silicon SH-Si and β-Sn silicon with 0.32 eV/atom and 0.29 eV/atom higher than that of diamond Si have also been synthesized [27,49]. But even so, it should be noted that the realization of $I4_1/acd$-Si_{80} experimentally may be a challenge due to its high-energy metastable feature.

The electronic band structures along the high symmetric lines in the Brillouin zone (BZ) [Fig. 3(b)] of $I4_1/acd$-Si_{80} calculated by gt-TB (blue) are presented in Fig. 3(a). It shows that highest valence band (HVB) crosses with the lowest conduction band (LCB) near the Fermi level along the Γ-X, M-Γ, and Γ-Z lines, which results in three Dirac cones on these lines. To understand the characteristics of these crossing states, the orbital and charge properties of HVB and LCB are studied. According to the orbital projections of HVB and LCB by TB, we can see that these two bands are mainly from the Si-s and Si-p_z orbitals and intersect with each other near the Γ point. The charge densities of A and B points at the two sides of the crossing point on M-Γ are calculated and displayed in Figs. 3(c) and 3(d) as an example, and it is found that the s

orbital are mainly from the Si_3 and Si_5 atoms while the p_z states are mainly from the Si_5 atoms. The band structure of $I4_1/acd$-Si_{80} is further identified by DFT-HSE as shown in Fig. 3(a) in red lines. It is clear that both of the band crossings and orbital projections from DFT-HSE are consistent with that of gt-TB, which not only confirms the Dirac-like states near Fermi level but also indicates that gt-TB can describe the band feature correctly.

It is interesting to see from the positions of the Dirac points around Γ that these Dirac points are in different high symmetric directions and planes in k space, which suggests that there may be some other Dirac points or band crossing points in the BZ. Therefore, we calculated the bands near Fermi level systemically to investigate the possible Dirac points and their distributions. As Γ-X and M-Γ are the two different high-symmetric lines of the M-Γ-X plane [p_v plane in Fig. 3(b)], we first calculated the TB band structure of $I4_1/acd$-Si_{80} with very high density k points of this plane. To find the possible Dirac points, the energy difference between LCB and HVB ($\Delta E = E_{LCB} - E_{HVB}$) was calculated and projected on the p_v plane [upper panel of Fig. 4(a)] and it clearly shows that there is a Dirac nodal ring ($\Delta E < 0.001$ eV) as denoted by the white circle. To confirm this Dirac nodal ring (DNR), we plotted the 3D band structure around Γ from the k points on the p_v plane [lower panel of Fig. 4(a)] and it is clear that the Dirac nodal ring is formed by the crossing of the HVB and LCB in the BZ. For the Z-Γ $-$ X_1 plane [the p_h plane in Fig. 3(b)], the projected ΔE and the 3D band structure around Γ show that there is also a Dirac nodal ring on the p_h plane around Γ. Combining these DNRs and the crystal symmetries, it suggests that a Dirac nodal sphere near the Γ point may be formed by DNRs. To confirm the existence of the DNS, we searched the k points in the BZ around Γ with $\Delta E \approx 0$ systematically and visualized in k space schematically in Fig. 4(c). It is found that these k points with almost zero band gap form a three-dimensional sphere, which verifies the Dirac nodal sphere around Γ. Furthermore, we analyze the symmetric properties of the Bloch states for the two crossing bands along the high symmetric lines. As stated before, the space group of the Dirac nodal sphere silicon allotrope is $I4_1/acd$ and it has 32 symmetry operations. According to the little irreducible representations along high-symmetric lines and the eigenvalues of the symmetry operators [50], we find that the DNLs are protected by the glide symmetries. For
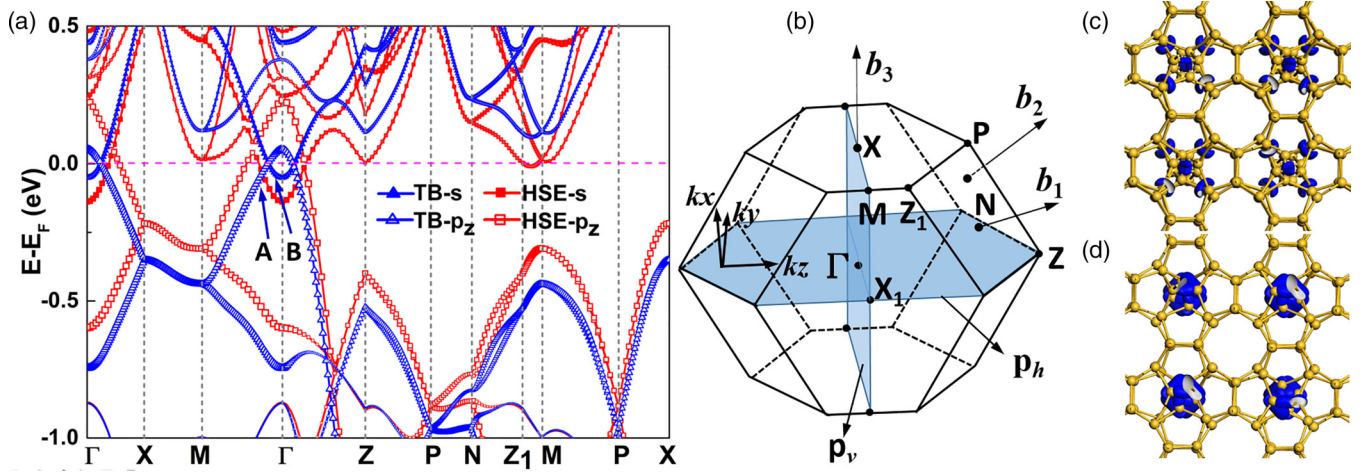
FIG. 3. (a) Band structure of I4$_1$/acd-Si$_{80}$ by TB and DFT-HSE along the high symmetry lines in Brillouin zone (b). (c) and (d) are the decomposed charge density of the state A and B labeled along M-Γ.

example, the little irreducible representations along Γ-X are DT$_1$ and DT$_2$ as presented in Fig. 4(d), and the eigenvalues of glide operators are opposite at the two sides of the Dirac nodal point. The symmetric properties along other directions are similar with that of Γ-X. These results show that besides the inversion and mirror symmetries, the PDNS states can also be realized by glide symmetry, which further improves the understanding about the symmetric properties of PNDS and is also useful for exploring PNDS in the future. It is noticed that the Dirac nodal sphere should be pseudo-Dirac nodal sphere as there are tiny band gaps (<1 meV) for the k points off high symmetric lines [as shown in the inset of Fig. 4(d)]. The PDNS feature can be well preserved under the spin-orbital coupling (SOC) effects, as the SOC effects in silicon are very weak and can be ignored.

The photoelectric properties of I4$_1$/acd-Si$_{80}$ are further studied as it plays important roles in applications of semimetals, such as detection of the chirality of Weyl fermion [51], bulk photovoltaic effect (BPVE) [52], and robust edge photocurrent [53]. The imaginary part of complex dielectric function $\varepsilon_2(\omega)$ based on the direct interband transitions [54] is calculated by

$$\varepsilon^{(2)}_{\alpha\beta} = \frac{4\pi^2 e^2}{\Omega} \lim_{q \to 0} \frac{1}{q^2} \sum_{c,v,\mathbf{k}} 2w_k \delta(\varepsilon_{c\mathbf{k}} - \varepsilon_{v\mathbf{k}} - \omega)$$

$$\times \langle u_{c\mathbf{k}+e_\alpha \mathbf{q}} | u_{v\mathbf{k}} \rangle \langle u_{c\mathbf{k}+e_\beta \mathbf{q}} | u_{v\mathbf{k}} \rangle^*, \qquad (1)$$

where the conduction and valence states are labeled by c and v. $u_{c\mathbf{k}}$, Ω, and ω are the cell periodic part of the wavefunctions at $\mathbf{k}$, the unit cell volume, and the photon energy,
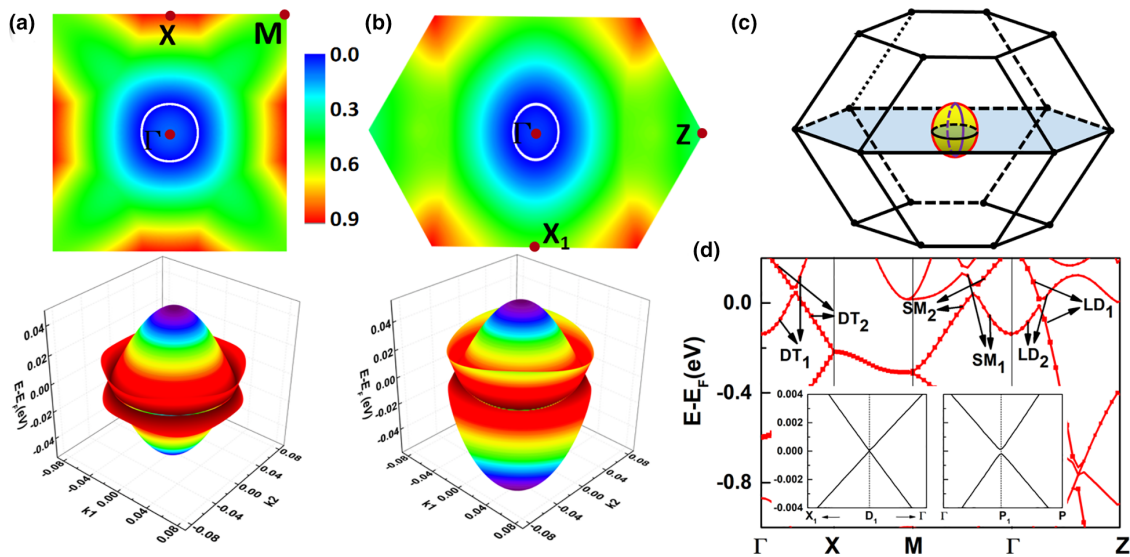
FIG. 4. Energy difference between the LCB and HVB (upper panel) and 3D Dirac nodal loop (lower panel) in the M-Γ-X plane (a) and Z-Γ-X$_1$ plane (b). (c) The schematic picture of the pseudo Dirac nodal sphere in the Brillouin zone. (d) Band structure of I4$_1$/acd-Si$_{80}$ with little irreducible representations along high symmetry lines.
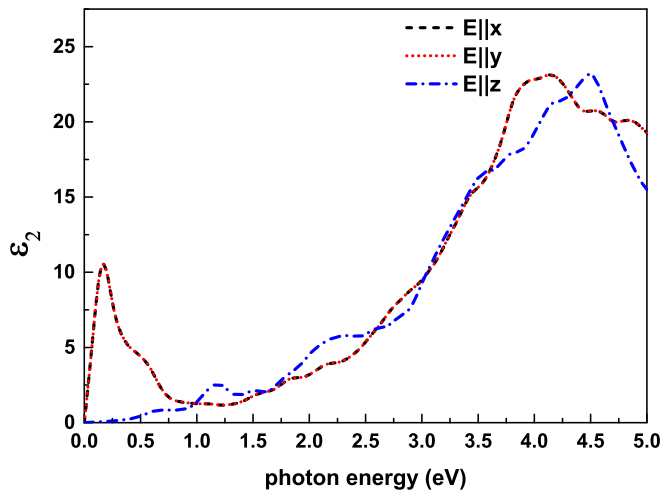
FIG. 5. The imaginary part of the dielectric function $\varepsilon_2(\omega)$ of $I4_1/acd$-Si_{80}.

respectively. The vectors e are unit vectors for the three Cartesian directions and the wave vector q of the incident electromagnetic wave. The calculated $\varepsilon_2(\omega)$ by the HSE-DFT is presented in Fig. 5. It can be seen that the dielectric functions of $I4_1/acd$-Si_{80} along x and y directions are the same but are significantly different with that of the z direction due to the fourfold screw symmetries along the z direction, indicating a strong anisotropic feature. Except for the strong absorption in the energy range of 2.0 eV to 4.5 eV, $I4_1/acd$-Si_{80} also shows apparent photoresponse from 0 to 0.5 eV. To understand the origin of the photoresponse in the low energy region, we have studied the properties of the electronic band structure [Fig. 3(a)] and the electronic transitions, and find that this photoresponse is contributed by the direct interband transitions between valence and conduction bands of the k points near the Dirac nodal sphere, which indicates that the Dirac electrons and holes can be induced by light. To investigate the properties of the Dirac fermion near PDNS, the Fermi velocities are estimated by $v_f = E(k)/\hbar|k|$, where $E(k)$ are the eigenvalues

of the corresponding k point from DFT-HSE. It is found that the Dirac fermion around the nodal sphere possesses very high Fermi velocity, for example, the v_f of the conduction band along Γ-X and Γ-Z near the Dirac point are 2.62×10^5 m/s and 6.5×10^5 m/s, respectively. These results suggest that $I4_1/acd$-Si_{80} has potential applications in high-speed Si-based photoelectric devices.

IV. CONCLUSIONS

In conclusion, we predict a silicon allotrope $I4_1/acd$-Si_{80} with pseudo-Dirac nodal sphere electronic properties by high-throughput screening based on RG^2 code and transferable DFT-HSE based tight-binding (TB) method. Phonon dispersion, *ab initio* molecular dynamics £¬elastic constants, and formation energy calculations reveal that $I4_1/acd$-Si_{80} is a metastable phase of silicon as its formation energy is about 0.22 eV higher than that of diamond Si. Furthermore, $I4_1/acd$-Si_{80} possesses the photoexcitable high Fermi velocity Dirac fermions near the Dirac nodal sphere, which suggests that $I4_1/acd$-Si_{80} has potential applications for Si-based high-speed photoelectric devices.

[1] X. G. Wan, A. M. Turner, A. Vishwanath, and S. Y. Savrasov, Topological semimetal and Fermi-arc surface states in the electronic structure of pyrochlore iridates, Phys. Rev. B **83**, 205101 (2011).

[2] A. A. Burkov, Topological semimetals, Nat. Mater. **15**, 1145 (2016).

[3] Q. Wei, X. W. Zhang, W. Y. Deng, J. Y. Lu, X. Q. Huang, M. Yan, G. Chen, Z. Y. Liu, and S. T. Jia, Higher-order topological semimetal in acoustic crystals, Nat. Mater. **20**, 812 (2021).

[4] Z. K. Liu, B. Zhou, Y. Zhang, Z. J. Wang, H. M. Weng, D. Prabhakaran, S. K. Mo, Z. X. Shen, Z. Fang, X. Dai, Z. Hussain, and Y. L. Chen, Discovery of a three-dimensional topological Dirac semimetal, Na$_3$Bi, Science **343**, 864 (2014).

[5] B. Q. Lv, T. Qian, and H. Ding, Experimental perspective on three-dimensional topological semimetals, Rev. Mod. Phys. **93**, 025002 (2021).

[6] A. Bernevig, H. M. Weng, Z. Fang, and X. Dai, Recent progress in the study of topological semimetals, J. Phys. Soc. Jpn. **87**, 041001 (2018).

[7] N. P. Armitage, E. J. Mele, and A. Vishwanath, Weyl and Dirac semimetals in three-dimensional solids, Rev. Mod. Phys. **90**, 015001 (2018).

[8] C. Fang, H. M. Weng, X. Dai, and Z. Fang, Topological nodal line semimetals, Chin. Phys. B **25**, 117106 (2016).

[9] Q.-F. Liang, J. Zhou, R. Yu, Z. Wang, and H. M. Weng, Node-surface and node-line fermions from nonsymmorphic lattice symmetries, Phys. Rev. B **93**, 085427 (2016).

[10] W. K. Wu, Y. Liu, S. Li, C. Y. Zhong, Z.-M. Yu, X.-L. Sheng, Y. X. Zhao, and S. A. Yang, Nodal surface semimetals: Theory and material realization, Phys. Rev. B **97**, 115125 (2018).

[11] T. Bzdušek, M. Sigrist, Robust doubly charged nodal lines and nodal surfaces in centrosymmetric systems, Phys. Rev. B **96**, 155105 (2017).

[12] J. F. Wang, Y. Z. Liu, K. Jin, X. L. Sui, L. Z. Zhang, W. H. Duan, F. Liu, and B. Huang, Pseudo Dirac nodal sphere semimetal, Phys. Rev. B **98**, 201112(R) (2018).

[13] R. González-Hernández, C. Pinilla, and B. Uribe, Quasinodal spheres and the spin Hall effect: The case of YH_3 and CaTe, Phys. Rev. B **106**, 125135 (2022).

[14] S. Z. Chen, S. W. Li, Y. P. Chen, and W. H. Duan, Nodal flexible-surface semimetals: Case of carbon nanotube networks, Nano Lett. **20**, 5400 (2020).

[15] S. Wippermann, Y. He, M. Vörös, and G. Galli, Novel silicon phases and nanostructures for solar energy conversion, Appl. Phys. Rev. **3**, 040807 (2016).

[16] G. K. Ramachandran, P. F. McMillan, S. K. Deb, M. Somayazulu, J. Gryko, J. J. Dong, and O. F. Sankey, High-pressure phase transformation of the silicon clathrate Si_{136}, J. Phys.: Condens. Matter **12**, 4013 (2000).

[17] L. Rapp, B. Haberl, C. J. Pickard, J. E. Bradby, E. G. Gamaly, J. S. Williams, and A. V. Rode, Experimental evidence of new tetragonal polymorphs of silicon formed through ultrafast laser-induced confined microexplosion, Nat. Commun. **6**, 7555 (2015).

[18] D. Y. Kim, S. Stefanoski, O. O. Kurakevych, and T. A. Strobel, Synthesis of an open-framework allotrope of silicon, Nat. Mater. **14**, 169 (2015).

[19] T. B. Shiell, and T. A. Strobel, Compression of sodium-filled and empty open-framework Si_{24} under quasihydrostatic and nonhydrostatic conditions, Phys. Rev. B **102**, 094107 (2020).

[20] M. Guerette, M. D. Ward, L. Zhu, and T. A. Strobe, Single-crystal synthesis and properties of the open-framework allotrope Si_{24}, J. Phys.: Condens. Matter **32**, 194001 (2020).

[21] Z. S. Zhao, F. Tian, X. Dong, Q. Li, Q. Q. Wang, H. Wang, X. Zhong, B. Xu, D. L. Yu, J. L. He, H. T. Wang, Y. M. Ma, and Y. J. Tian, Tetragonal allotrope of group 14 elements, J. Am. Chem. Soc. **134**, 12362 (2012).

[22] H. J. Xiang, B. Huang, E. Kan, S. H. Wei, and X. G. Gong, Towards direct-gap silicon phases by the inverse band structure design approach, Phys. Rev. Lett. **110**, 118702 (2013).

[23] Q. Q. Wang, B. Xu, J. Sun, H. Y. Liu, Z. S. Zhao, D. L. Yu, C. Z. Fan, and J. L. He, Direct band gap silicon allotropes, J. Am. Chem. Soc. **136**, 9826 (2014).

[24] C. Y. He, X. Z. Shi, S. J. Clark, J. Li, C. J. Pickard, T. Ouyang, C. X. Zhang, C. Tang, and J. X. Zhong, Complex low energy tetrahedral polymorphs of group IV elements from first principles, Phys. Rev. Lett. **121**, 175701 (2018).

[25] H. J. Sung, W. H. Han, I. H. Lee, and K. J. Chang, Superconducting open-framework allotrope of silicon at ambient pressurem, Phys. Rev. Lett. **120**, 157001 (2018).

[26] Z. F. Liu, H. L. Xin, L. Fu, Y. Q. Liu, T. L. Song, X. Cui, G. J. Zhao, and J. J. Zhao, All-silicon topological semimetals with closed nodal line, J. Phys. Chem. Lett. **10**, 244 (2019).

[27] L. Y. Su, S. F. Li, J. Li, C. Y. He, X. T. Zeng, X. L. Sheng, T. Ouyang, C. X. Zhang, C. Tang, and J. X. Zhong, $I4/mcm$-Si_{48}: An ideal topological nodal-line semimetal, ACS Mater. Lett. **4**, 1726 (2022).

[28] S. Curtarolo, G. L. W. Hart, M. B. Nardelli, N. Mingo, S. Sanvito, and O. Levy, The high-throughput highway to computational materials design, Nat. Mater. **12**, 191 (2013).

[29] R. Gómez-Bombarelli, J. Aguilera-Iparraguirre, T. D. Hirzel, D. Duvenaud, D. Maclaurin, M. A. Blood-Forsythe, H. K. Chae, M. Einzinger, D. G. Ha, T. Wu, G. Markopoulos, S. Jeon, H. Kang, H. Miyazaki, M. Numata, S. Kim, W. L. Huang, S. I. Hong, M. Baldo, R. P. Adams *et al.*, Design of efficient molecular organic light-emitting diodes by a high-throughput virtual screening and experimental approach, Nat. Mater. **15**, 1120 (2016).

[30] X. Z. Shi, S. F. Li, J. Li, T. Ouyang, C. X. Zhang, C. Tang, C. Y. He, and J. X. Zhong, High-throughput screening of two-dimensional planar sp^2 carbon space associated with a labeled quotient graph, J. Phys. Chem. Lett. **12**, 11511 (2021).

[31] X. Shi, C. Y. He, C. J. Pickard, C. Tang, and J. X. Zhong, Stochastic generation of complex crystal structures combining group and graph theory with application to carbon, Phys. Rev. B **97**, 014104 (2018).

[32] Z. H. Gong, X. Z. Shi, J. Li, S. F. Li, C. Y. He, T. Ouyang, C. X. Zhang, C. Tang, and J. X. Zhong, Theoretical prediction of low-energy Stone-Wales graphene with an intrinsic Type-III Dirac cone, Phys. Rev. B **101**, 155427 (2020).

[33] J. Li, S. F. Li, T. Ouyang, C. X. Zhang, C. Tang, C. Y. He, J. X. Zhong, Two-dimensional carbon allotropes and nanoribbons based on 2, 6-polyazulene chains: Stacking stabilities and electronic properties, J. Phys. Chem. Lett. **12**, 732 (2021).

[34] G. Kresse, J. Furthmüller, Efficient iterative schemes for ab initio total-energy calculations using a plane-wave basis set, Phys. Rev. B **54**, 11169 (1996).

[35] P. E. Blöchl, Projector augmented-wave method, Phys. Rev. B **50**, 17953 (1994).

[36] J. P. Perdew, K. Burke, and M. Ernzerhof, Generalized gradient approximation made simple, Phys. Rev. Lett. **77**, 3865 (1996).

[37] J. Heyd, G. E. Scuseria, and M. Ernzerhof, Hybrid functionals based on a screened Coulomb potential, J. Chem. Phys. **118**, 8207 (2003).

[38] A. A. Mostofi, J. R. Yates, Y. S. Lee, I. Souza, D. Vanderbilt, and N. Marzari, wannier90: A tool for obtaining maximally-localised Wannier functions, Comput. Phys. Commun. **178**, 685 (2008).

[39] A. Togo, F. Oba, and I. Tanaka, First-principles calculations of the ferroelastic transition between rutile-type and $CaCl_2$-type SiO_2 at high pressures, Phys. Rev. B **78**, 134106 (2008).

[40] Z. J. Wu, E. J. Zhao, H. P. Xiang, X. F. Hao, X. J. Liu, and J. Meng, Crystal structures and elastic properties of superhard IrN_2 and IrN_3 from first principles, Phys. Rev. B **76**, 054115 (2007).

[41] X.-L. Sheng, Q.-B. Yan, F. Ye, Q.-R. Zheng, and G. Su, T-carbon: A novel carbon allotrope, Phys. Rev. Lett. **106**, 155703 (2011).

[42] J. Zhang, R. Wang, X. Zhu, A. Pan, C. Han, X. Li, D. Zhao, C. Ma, W. Wang, H. Su, and C. Niu, Pseudo-topotactic conversion of carbon nanotubes to T-carbon nanowires under picosecond laser irradiation in methano, Nat. Commun. **8**, 683 (2017).

[43] K. Yamada, Shock synthesis of a new cubic form of carbon, Carbon **41**, 1309 (2003).

[44] C. He, C. X. Zhang, H. Xiao, L. Meng, and J. X. Zhong, New candidate for the simple cubic carbon sample shock-synthesized by compression of the mixture of carbon black and tetracyanoethylene, Carbon **112**, 91 (2017).

[45] R. Matsuoka, R. Sakamoto, K. Hoshiko, S. Sasaki, H. Masunaga, K. Nagashio, and H. Nishihara, Crystalline graphdiyne nanosheets produced at a gas/liquid or liquid/liquid interface, J. Am. Chem. Soc. **139**, 3145 (2017).

[46] B. Li, C. Lai, M. Zhang, G. Zeng, S. Liu, D. Huang, L. Qin, X. Liu, H. Yi, F. Xu, N. An, and L. Chen, Graphdiyne: A rising star of electrocatalyst support for energy conversion, Adv. Energy Mater. **10**, 2000177 (2020).

[47] Q. Fan, L. Yan, M. W. Tripp, O. Krejči, S. Dimosthenous, S. R. Kachel, M. Chen, A. S. Foster, U. Koert, P. Liljeroth, and J. M. Gottfried, Biphenylene network: A nonbenzenoid carbon allotrope, Science **372**, 852 (2021).

[48] Y. Luo, C. Ren, Y. Xu, J. Yu, S. Wang, and M. Sun, A first principles investigation on the structural, mechanical, electronic, and catalytic properties of biphenylene, Sci. Rep. **11**, 19008 (2021).

[49] A. Mujica, Angel Rubio, A. Muñoz, and R. J. Needs, High-pressure phases of group-IV, III–V, and II–VI compounds, Rev. Mod. Phys. **75**, 863 (2003).

[50] J. C. Gao, Q. S. Wu, C. Persson, and Z. J. Wang, Irvsp: To obtain irreducible representations of electronic states in the VASP, Comput. Phys. Commun. **261**, 107760 (2021).

[51] Q. Ma, S. Y. Xu, C. K. Chan, C. L. Zhang, G. Q. Chang, Y. X. Lin, W. W. Xie, T. Palacios, S. Lin, S. Jia, P. A. Lee, P. Jarillo-Herrero, and N. Gedik, Direct optical detection of Weyl fermion chirality in a topological semimetal, Nat. Phys. **13**, 842 (2017).

[52] G. B. Osterhoudt, L. K. Diebel, M. J. Gray, X. Yang, J. Stanco, X. W. Huang, B. Shen, N. Ni, P. J. W. Moll, Y. Ran, and K. S. Burch, Colossal mid-infrared bulk photovoltaic effect in a type-I Weyl semimeta, Nat. Mater. **18**, 471 (2019).

[53] Q. S. Wang, J. C. Zheng, Y. He, J. Cao, X. Liu, M. Y. Wang, J. C. Ma, J. W. Lai, H. Lu, S. Jia, D. Y. Yan, Y. G. Shi, J. X. Duan, J. F. Han, W. D. Xiao, J. H. Chen, K. Sun, Y. G. Yao, and D. Sun, Robust edge photocurrent response on layered type II Weyl semimetal WTe$_2$, Nat. Commun. **10**, 5736 (2019).

[54] M. Gajdoš, K. Hummer, G. Kresse, J. Furthmüller, and F. Bechstedt, Linear optical properties in the projector-augmented wave methodology, Phys. Rev. B **73**, 045112 (2006).